

Preliminary Report on the 28 September 2004, M 6.0 Parkfield, California Earthquake

John Langbein¹, Roger Borchardt¹, Douglas Dreger², Joe Fletcher¹, Jeanne L. Hardebeck¹, Margaret Hellweg², Chen Ji³, Malcolm Johnston¹, Jessica R. Murray¹, Robert Nadeau², Michael J. Rymer¹, Jerome A. Treiman⁴

*Submitted to SRL
November 5, 2004*

¹ US Geological Survey, Menlo Park, CA 94025

² UC Berkeley, Berkeley, CA

³ California Institute of Technology, Pasadena, CA

⁴ California Geological Survey, Los Angeles, CA

Introduction

The M_w 6.0 Parkfield earthquake struck central California at 17:15:14 UTC on 28 September 2004. The epicenter was located 11 km southeast of the rural town of Parkfield adjacent to Gold Hill and on the San Andreas Fault (Figure 1). The California Integrated Seismic Network (CISN) reported that the hypocenter is located at 35.819°N, 120.364°W at a depth of 8.8 km. From the distribution of aftershocks and from models of seismograms, strain changes, and geodetic displacements from the earthquake, it appears that the rupture propagated to the northwest along the San Andreas fault from its hypocenter beneath Gold Hill to Middle Mountain. Because of the earthquake's moderate size and the low population density, there was only minimal reported damage; however, strong ground motions of approximately 1 g were recorded at a few isolated points (Shakal, this volume).

The 2004 Parkfield earthquake is the sixth of a series of historical events located on this reach of the San Andreas Fault; similar-sized earthquakes occurred in 1881, 1901, 1922, 1934, and 1966 (Bakun and McEvilly, 1984). Because of the frequency of moderate-sized earthquakes in the same locality, the Parkfield Prediction Experiment (Bakun and Lindh, 1985) was initiated in the mid-1980's, with cooperation between the US Geological Survey (USGS), the California Geological Survey (CGS), and various universities to instrument the area densely to capture a future earthquake. In addition to enlarging the seismic network with more short-period, broadband, and strong motion instruments, other instruments were installed that are unique to this experiment. These instruments include borehole strainmeters, Global Positioning System (GPS) receivers, a borehole seismic network, creepmeters, a telluric array, magnetometers, and fluid pressure sensors (Roeloffs and Langbein, 1994). The goal of the experiment was to capture the complete earthquake cycle: the inter-seismic period, the actual earthquake, and the post-seismic response. The locations of the GPS stations, borehole strainmeters, magnetometers, and creepmeters are shown in Figure 2.

The Parkfield earthquakes are located on the San Andreas Fault, which is the primary transform fault that accommodates motion between the Pacific and North American plates. The Parkfield section is transitional between the creeping section to the northwest and the locked section to the southeast. Fault creep northwest of Parkfield averages 25 mm/yr of right-lateral slip, and earthquakes in the creeping section tend to be limited to magnitude 5 or less. Southeast of Parkfield, the fault is locked and last broke in the M7.9, Fort Tejon Earthquake in 1857. Historical evidence suggests that at least one M6 earthquake at Parkfield preceded the great 1857 event by 1 to 2 hours (Meltzner and Wald, 1999). Although the large 1857 event had roughly 6 meters of offset in southern California, there is some geologic evidence suggesting that the Cholame fault segment, located just southeast of Parkfield, slipped only 3 meters in 1857 indicating incomplete stress release on this segment. Consequently, Sieh and Jahns, (1984), and Harris and Archuleta (1988) speculated that a future Parkfield earthquake could be a foreshock to a larger Cholame earthquake, or could nucleate a larger event that propagates to the southeast into the Cholame segment.

Bakun and McEvilly (1984) noted an apparent 22-year regularity of repeating events starting

with the 1857 earthquake. In addition, comparisons by Bakun and McEvelly (1979) of seismograph recordings of the 1922, 1934, and 1966 events suggested that all three events nucleated near the same place under Middle Mountain and propagated to the southeast. Based upon the regularity and the similarity, a long-term prediction was issued in 1985 for another Parkfield earthquake to occur between 1985 and 1993. However, the anticipated earthquake did not occur within the prediction window. Speculation continues about the unsuccessful prediction, with arguments centering about the probability distribution of so-called characteristic earthquakes, the effect of the M7.9, 1857 earthquake on the timing of Parkfield earthquakes, and the effect of the 1983, M6.5 Coalinga earthquake on the accumulation of stress at Parkfield. Models by Ben-Zion et al. (1993) of the M7.9 1857 earthquake suggest that the repeat times between successive Parkfield earthquakes should get longer. In addition, models of the distribution of stresses imposed on the San Andreas Fault near Parkfield by the Coalinga earthquake suggest that that event might have delayed the occurrence of the Parkfield earthquake (Simpson et al., 1989; Toda and Stein, 2002).

Because of the density and diversity of instrumentation located at Parkfield, the quality and the quantity of data recorded from the 2004 event are unique and should provide new insights into the many aspects of the earthquake cycle. Discussed below are many of the observations and preliminary inferences about the 2004 earthquake and comparisons between this event and prior Parkfield events.

Comparison with Previous Parkfield earthquakes

Bakun and McEvelly (1979) compared seismograms from the 1934 and 1966 Parkfield earthquakes written by the north component of the Wood-Anderson seismographs at MHC, TIN and SBC. Seismograms from MHC and SBC taken from that paper (Figure 3) show very clearly the similarity between the 1934 and 1966 earthquakes. Figure 3 also shows simulated Wood-Anderson seismograms from the 2004 event calculated from the broadband recordings at these same stations. When the initial pulses in the seismograms are aligned (dashed lines), the later arrivals in the 2004 seismograms are earlier at MHC and later at SBC than in the records from the 1934 and 1966 earthquakes. These arrival time differences would be expected for an event rupturing to the NW (2004) compared to an event rupturing to the SE (1934 and 1966) since both of these stations lie along the direction of rupture, MHC to the NW and SBC to the SE. However, this explanation is not unique. For instance, differing focal depths can refract later phase arrivals (Bakun, 1972) and produce similar observations as those in Figure 3.

Aftershocks

The distribution of aftershocks from the 2004 Parkfield earthquake quickly established that the rupture was located between Gold Hill and Middle Mountain (Figures 2 and 4). The locations of some of the largest aftershocks are shown in Figure 4 with a M_L 4.7 occurring 9 minutes after the mainshock and two, M_w 5.0 events following within two days of the mainshock and located at the north end of the rupture zone beneath Middle Mountain.

The aftershocks, along with selected background earthquakes, were relocated to determine their absolute and relative positions. The absolute locations were found from the CISN phase data using the program SIMULPS (Evans et al., 1994) and the 3D seismic velocity model for the Parkfield region determined by Michael and Eberhart-Phillips (1991) and Eberhart-Phillips and Michael (1993). Their station corrections were used, and additional corrections were found for stations not included in their study by minimizing the travel time residuals. Because of the velocity contrast across the San Andreas Fault, absolute locations determined using a 1D, layered model are shifted towards the higher-velocity crust, in this case to the SW. The 3D velocity model includes the across-fault velocity contrast, and therefore produces more accurate locations. The relative event locations were then refined using the double-difference method of Waldhauser and Ellsworth (2000), using only catalog phase data since waveform cross-correlations have not yet been performed. A total of 630 aftershocks from the first 2 weeks, M0.8-5.0, were relocated, as well as 2039 background events, M1.0-5.1, that occurred during 1969-2004.

The spatial distribution of the aftershocks is very similar to that of the background seismicity (Figure 4). More specifically, the background earthquakes tend to cluster, and the aftershocks occur in these same patches (Figure 5). Both the aftershocks and the background seismicity in the epicentral region are offset to the SW from the main surface trace of the San Andreas where long-term creep is observed, and align more closely with the mapped southwest fracture zone (SWFZ, Figure 4) which had ground breakage from the 2004 event. This shift could be caused by an underestimated velocity contrast across the fault. The geometry of the fault strands at depth is not known, so it is unclear how the seismogenic structure at depth is related to the main trace and SW fracture zone at the surface.

Observations of surface rupture and post-mainshock surface slip

Surface fracturing occurred along the San Andreas Fault, the subparallel southwest fracture zone, and secondary faults in association with the 2004 Parkfield earthquake. Field checks near Parkfield and about 5 km to the southeast indicate that surface fractures began to develop more than 1 hour but less than 1 day after the mainshock.

To measure amounts and locations of afterslip, nail quadrilaterals were installed at 10 sites across the San Andreas, SWFZ, and one secondary fault. Repeated measurements of these quadrilaterals indicate that afterslip 1) is located only along the San Andreas Fault, 2) is ongoing at the time of this writing, and 3) at least locally, constitutes a significant amount of the total surface slip. These observations are consistent with those from creepmeters reported below.

Field mapping reveals that fractures formed discontinuous breaks along at least a 32-km-long stretch of the San Andreas Fault; additional fresh surface breakage was observed extending farther northwest towards SAFOD (Figure 6) and into an area of extensive landslides. Dextral slip ranged from 1 to 44 mm and was greatest in the Middle Mountain area. There was a minor

(1 to 11 mm) vertical component of slip. Slip on the SWFZ extended at least 8 km with dextral slip ranging from 1 to 41 mm with the maximum adjacent to Carr Hill and the CARH GPS receiver (see below). Locally, there was a vertical component of slip (1 to 29 mm) on the SWFZ. Surface slip on secondary faults extended only short distances, about 10 to 50 m with the right-lateral component of slip ranging from 1 to 7 mm, and a minor (1 to 2 mm) vertical component of slip.

Comparisons of surface slip in 2004 with slip in 1966 (Brown et al., 1967; and Lienkaemper and Brown, 1985) show many similarities and some differences. Slip in both events was on the San Andreas and SWFZ. Mapped fractures on the San Andreas Fault extended southeast of Gold Hill in 1966, but not in 2004. To date, the observations suggest that the surface slip in 2004 on the San Andreas is about half of that seen in 1966. The length of ground breakage along the SWFZ was the same in 1966 and 2004, but right-lateral slip amounts in 2004 were about twice those in 1966. Also, surface fractures were more continuous on the SWFZ in 2004 than in 1966.

Pre-seismic Observations

During the week to minutes before the earthquake, there were no indications of changes in fault creep or microseismicity. Only very small (10 nanostrain or less) strain change occurred at some sites during the last 24 hours prior to the mainshock (Figure 7). Although intriguing, strain changes of this amplitude occurring over this time period are not significantly different from background variations. During the 20 seconds before the event (Figure 8), recorded strain was stable at the 10^{-10} level. Assuming a stress drop of 3 MPa, this constrains the moment of any prerupture nucleation in the hypocentral region during the 20 seconds before the earthquake to less than 7×10^{13} Nm (M3.2). The source size would have to be less than 100 m consistent with observations for other earthquakes elsewhere in the San Andreas system (Johnston and Linde, 2002).

Precise measurements of local magnetic fields have been obtained with a differentially connected array of seven synchronized proton magnetometers in the Parkfield region since 1984 (Johnston et al., 1983). Telluric electric fields and apparent resistivity have been monitored in the same region since 1986 (Park, 1997). Although the mainshock generated co-seismic magnetic field steps of between 0.2 and 0.5 nT at about half the magnetometers in the network, and 1-2 mV in telluric potential field, no apparent resistivity changes were associated with the earthquake. Moreover, during the month, week, and days prior to the earthquake, there were no detectable changes in telluric electric field or apparent resistivity. and magnetic field changes are not apparent at the 0.5 nT level.

Also absent in terms of pre-seismic signals are any small earthquakes occurring in the epicentral area that could be identified as foreshocks. Neither the records from the NCSN nor from UC Berkeley's 13-station borehole seismic network detected any earthquake greater than M0 for the 6 days before to the mainshock in the region between Gold Hill and Middle Mountain. However, in the preceding 7 to 10 days there were three shallow microearthquakes

that occurred on the fault segment between Parkfield and Middle Mountain and several additional microearthquakes located in the vicinity of the SAFOD site (Figure 1) and along the fault to the northwest. All of these microearthquakes are considered typical, background seismicity.

In the hypocentral area beneath Gold Hill, there is very low seismicity in the 35 years leading up to the 2004 earthquake (Waldhauser and Ellsworth, 2004; Figure 5). Only 11 events occurred with 1 km of the hypocenter, the largest of which being a M3.0 event that occurred in 1986.

Source Modeling

The seismic moment tensor for the mainshock and large aftershocks, determined using the automated, complete waveform method (Pasyanos et al., 1996), are dominated by double-couple components. Figure 4 shows the dominant double-couple components of the moment tensor solutions for the mainshock and 4 of the largest aftershocks. For the mainshock, the focal parameters were found to be as follows: a scalar moment of 9.97×10^{17} Nm (M_w 6.0); strike, rake and dip of N140°E, -172°, 77°; and centroid-depth of 8 km. This solution is based on fitting 50 to 20 second period, three-component waveforms at the BDSN stations KCC, MHC, WENL and Caltech stations ISA and SBC.

The Parkfield dense seismic array, UPSAR, (Fletcher et al., 1992), a short baseline array located about 12 km west of Gold Hill (Figure 2), recorded the mainshock on 12 accelerometers with peak acceleration ranging up to 0.46g. This array was installed in the late 1980s to observe and to image the rupture propagation of the anticipated Parkfield earthquake. A preliminary analysis shows that rays arriving at the array after the direct S-wave from the hypocenter show time-dependent change in azimuth consistent with a northward propagating rupture. This result was determined using the method of Frankel et al. (1991) to determine slowness of incoming arrivals at small arrays comprised of 3 stations arranged in a triangular array with station spacing between 120 and 180 meters. Correlation of arrivals is computed over a range of slowness and high values of correlation are interpreted to be real arrivals at the array. On the north component, azimuths of peaks in correlation change from about 80° (due east of array) to about 50° over about 2.5 seconds. This change in azimuth is consistent with a line source at a depth of 8.5 km that propagates northwestward from beneath Gold Hill with a rupture velocity of 60% of the crustal shear wave velocity or 2.1 km/s.

Using different methods and different subsets of the data that span the earthquake, three models of the slip distribution have been obtained (Figure 9). The first model is determined from offsets in the GPS and borehole strainmeter data that span the period of the mainshock though 2 October 2004. The GPS data include offsets from both the continuous operating sites and 10 sites occupied shortly after the earthquake for which the most recent measurements were in 2001 or 2003 (Figure 10). The campaign sites were chosen to augment the poor coverage of the continuous network south of Gold Hill. The strainmeter data came from 4

dilatometers shown in Figure 10. To make the relative uncertainties of the strainmeter and GPS data about the same, the strainmeter uncertainties were increased and taken to be 10% of the observed, co-seismic strain. The second model is based upon seismic waveforms from 8 broadband seismic stations located within 300 km of Parkfield and from static offsets from the continuous GPS sites located near Parkfield (Figure 11). In contrast to the GPS offsets used for the first model, these offsets were estimated using the data taken within 6 hours after the mainshock and compared to those measurements taken 5 days prior to the mainshock (N. King, written communication 2004). The third model uses a combination of seismic waveform data from 2 nearby broadband stations and one strong motion station along with displacements measured at 1-second intervals from the continuous GPS stations at Parkfield (K. Choi, written communication, 2004, Larson et al., 2003 and Langbein and Bock, 2004). In addition, the static offsets used in the second model are also used for the third model. For both the second and third models, the seismic acceleration data was doubly integrated to obtain displacement.

In estimating the co-seismic displacements, neither the first nor second model includes the GPS site CARH (Figure 2). The co-seismic displacement at station CARH was more similar to that of stations east of the San Andreas Fault, even though this station is west of creeping, surface expression of the fault. The post-seismic displacement at CARH, however, is in keeping with its location west of the main trace. The complicated deformation at CARH might be related to the large co-seismic offsets seen on the nearby SWFZ immediately following the mainshock.

Using the method of Murray et al. (2001), the results from model 1 (Figure 9a) indicate that the majority of slip occurred between the hypocenter, beneath Gold Hill, and beneath Middle Mountain. The fault plane is assumed to be vertical and its surface projection is shown in Figure 10. The peak slip is 27 cm centered on the under the area between Carr Hill and Middle Mountain, and the moment of the imaged slip is 1.8×10^{18} N m. This is equivalent to an M_w 6.1 earthquake. In the solution, up to ~15 cm of slip is apparent at the surface near CARH, which exceed the observations from creepmeters. If displacements of shallow surface elements were constrained to agree with the creep observations, it is likely that the amplitude of estimated slip at depth would increase somewhat. The observed, GPS displacement vectors are shown in Figure 10 along with the predicted displacements from this model of slip.

For model 2, using a method based on Hartzell and Heaton (1983), the temporal model of rupture was divided into 12 overlapping window of 0.6-seconds each which yields an allowable range of 0.6 to 3.6 seconds in rise time. Maximum rupture velocities from 2 to 3.8 km/s were tested. The optimum rupture velocity was estimated by inverting only the seismic data and then using that model to predict the displacements measured by GPS. It was found that a rupture velocity of 3.2 km/s best fit both data sets. With this rupture velocity, the seismic waveform and GPS data were then inverted simultaneously to find the slip distribution. Although this rupture velocity faster than that obtained from the UPSAR data, it does agree with the combined seismic and GPS results obtained in model 3. Green's functions were computed using the GIL7 velocity model, which is used for seismic moment tensor analysis for events in the central Coast Ranges (Pasyanos et al., 1996). The GPS data were modeled assuming a half space model using an average rigidity based upon the GIL7 model. The fault

plane was assumed to have the strike of the San Andreas Fault and dips 80° to the southwest based on the preliminary seismic moment tensor solution. For the analysis presented here, it was assumed that slip is purely right-lateral.

The slip distribution for model 2 shown in Figure 9b has a scalar moment of 1.10×10^{18} Nm, average slip of 15.5 cm, peak slip of 91.5 cm, and an average stress drop of 0.56 Mpa. Slip is confined to three areas with most slip concentrated under the area between Carr Hill and Middle Mountain. Less slip is associated with the location of the mainshock beneath Gold Hill. A third patch of higher slip is in the middle of the fault at shallower depth. Inversions of the seismic data only reveal that this shallow slip is not needed to explain the seismic waveforms, but is required by the near-fault GPS data.

The fit of model 2 is shown for the GPS data in Figure 11 and for the seismic displacements in Figure 12. The fit to the seismic waveform data is good, particularly for the nearby sites. Stations PKD and SMM illustrate the predominant NW directivity in the event in terms of amplitude and duration of the waves. The more distant stations provide needed coverage, and although the distances are large, the fit to the data is also acceptable.

A third model constructed using the method of Ji et al. (2002) is shown in Figure 9c. The modeled fault plane dips 83° to the southwest based upon the moment tensor solution and it intersects the surface trace of the San Andreas Fault. A 1D velocity structure modified from a 3D velocity structure around Parkfield (Thurber et al., 2003) is used to calculate Green's functions of both static displacement and synthetic seismograms.

The total seismic moment of this third model is 9.4×10^{17} Nm, consistent with the point source moment tensor solution. For model 3, the earthquake ruptures towards northwest for about 22 km with a rupture velocity of 3.0 km/sec, which is also higher than the UPSAR estimate. The slip distribution is characterized by two slip-patches. One of them is around the hypocenter and has a peak slip of 42 cm. The slip is limited to a depth range from 6 to 11 km. The other is centered 15 km northwest of the epicenter and has a peak slip about 30 cm. The model explains the strong motion and 1-Hz GPS data reasonably well (Figure 13), but underestimates GPS vectors, suggesting significant afterslip in the static, GPS displacements.

In summary, all of the models reveal significant slip beneath the segment between Middle Mountain and Carr Hill. The two models derived using seismic waveform data yield relatively high velocities of 3.2 and 3.0 km/s in agreement with each other, but conflict with the UPSAR estimate of 2.1 km/s. Rupture velocity may have been variable along the length of the rupture; it is also likely that further, more in-depth analysis will yield revised rupture velocity estimates. Although the estimates of seismic moment varied by a factor of 2 between the 3 models, comparison of the seismic potency (product of ruptured area and average slip) deviates by only a factor of 1.5. Other features of the three models are not consistent with each other. Some of the differences can be explained by inclusion of the static GPS data. The combination of GPS and strainmeter data included in model 1 includes more of the post-seismic period than the other two models and this model had the largest seismic potency of the three. Different

weighting of the static GPS versus the high frequency GPS and seismic data might account for some of the differences between models 2 and 3. Other differences might be due to differences in the dip and the position of modeled fault plane, the allowance of variable slip direction in model 3 but not in model 2, and the assumed Earth structure models. Additional data, including the strong motion results described in Shakal et al. (this volume) and axillary data from additional 3-component seismometers and volumetric strainmeter data, recorded at 200 samples/second, will provide more details of the rupture process than the models presented here. Figure 14 shows an example of data (Borcherdt et al., 2004) obtained from the strainmeter site FR (Figure 2). The future models of the rupture process will have to predict the wide range and spatially variable peak accelerations observed in the Parkfield area (Shakal et al., this volume). Peak acceleration values up to 1.3 g were recorded at sites in the zone between Carr Hill and Middle Mountain at a distance of about 17 to 19 km north of the epicenter. Also, high accelerations, up to 0.8 g, were recorded at a few sites south of the rupture. These large values were significantly greater than measurements ranging between 0.2 and 0.4g recorded north and south of this region of the fault zone.

Post-seismic changes

Data from the creepmeters, continuous GPS sites, and borehole strainmeters all show post-seismic deformation. In Figure 15, the time series from 10 days before the earthquake to 20 days after the earthquake for three different instruments is shown as a representative sample of data from the creepmeter, GPS, and strainmeter networks. All of the instruments shown in Figure 15 have clear co-seismic and post-seismic displacements and, as of this writing (1 November 2004), all instruments still have continued, post-seismic movement. The sense of post-seismic deformation is the same as the co-seismic deformation, except for the case of the CARH GPS, as noted before. Interestingly, the post-seismic time-constant differs between the instruments. The data plotted in Figure 15 suggest that the strainmeter data have a shorter time-constant than GPS and creep. Less pronounced is that creep may have a longer time-constant than the GPS but more data will be needed to confirm this.

A high time-resolution examination of a few of the creepmeter records spanning the time of the earthquake is shown in Figure 16. For the sites XTA1, TABC, CRR1, and XGH1, all within 10 km of the epicenter, the measurements suggest that slip was initiated between 0.5 and 2 hours following the mainshock. This is consistent with the observation that no surface rupture was observed immediately after the mainshock. These four instruments are within 10 km of the mainshock. The instruments XMM1 and XMBC, which are collocated on Middle Mountain 20 km northwest of the mainshock, suggest immediate ground breakage with apparent slip between 1 and 2 cm. However, approximately 1.5 hours after the mainshock, a more gradual displacement commenced which is similar to the records of slip recorded at the other four sites. It is possible that the shaking from the mainshock caused the piers of the creepmeter at XMM1/XMBC to move; this type of offset has been seen at this site from a nearby explosion. Consequently, the initial, co-seismic offset at XMM1/XMBC may be due to transient shaking.

All of the creepmeters have a high, 0.01 mm, sensitivity but have a limited-range, 25 mm

displacement transducer. A few sites, however, have a low, 0.1mm, sensitivity but with greater range. In fact, slip as measured by the creepmeters at most of the sites northwest of the mainshock exceeded the maximum range of the high sensitivity sensor. By three days after the mainshock all of the high sensitivity creepmeters were again operational and, except for one site where its Invar wire broke, the total displacements were recovered using manual measurements. Where either the total slip was low, < 1 cm, or where the low-sensitivity sensor worked, high temporal resolution displacement data are available through the mainshock and the subsequent, rapid slip following the earthquake. For instance, the data for XMM1 in Figure 15 are from the low sensitivity sensor because the high sensitivity sensor was off-scale for part of the period.

Repeats of the two, M2 target event sequences (Nadeau et al., 2004) for the SAFOD (San Andreas Fault Observatory at Depth) experiment (Figure 1) occurred within 2 days of the Parkfield mainshock. Based on the pattern of recurrence for the previous 7 events in these sequences, their next repeats were not expected until late in 2006 (Nadeau et al., 2004). This observation has three important implications: 1) that the changes in the stress field from the M6 mainshock did not shut down the M2 target sequences and they remain viable targets for SAFOD's long-term monitoring plan, 2) that in the two days following the M6, ~ 3.3 cm of deep (~2.9 km) aseismic slip occurred on the fault surrounding the M2 targets (based on the aseismic slip loading to moment relationship of Nadeau and Johnson, (1998), and 3) that an accelerated rate of repetition of the M2 sequences can perhaps be expected in the near future as elevated afterslip load from the M6 continues to accumulate on the M2 sequence patches.

Discussion

The 2004 Parkfield earthquake had the same magnitude and ruptured approximately the same fault-segment of the San Andreas Fault as the 1922, 1934 and 1966 earthquakes suggesting that Parkfield earthquakes are, in some sense, characteristic based on magnitude and location. Little is known about Parkfield earthquakes before 1922. When these earthquakes are studied in detail, however, there are many differences. The 2004 earthquake started beneath Gold Hill and ruptured northwest toward Middle Mountain. In contrast, both the 1934 and the 1966 events initiated under Middle Mountain and propagated to the southeast towards Gold Hill; it is likely that the 1922 event ruptured like those in 1934 and 1966. In addition, Lindh and Boore (1981) concluded that the 1966 event stopped beneath Gold Hill. However, Segall and Du (1993) used geodetic data to infer that the 1966 shock differed from the 1934 event as the 1966 ruptured continued to the southeast of Gold Hill but 1934 did not. Comparison of the source models shown in Figure 9 for the 2004 event suggest that this event may be similar to the 1934 event in that both ruptured the fault segment between Middle Mountain and Gold Hill. However, the final analysis of this comparison will have to wait as more geodetic measurements are obtained for the post-seismic period following the 2004 event. The comparison of seismograms of the 1934 and 1966 events by Bakun and McEvilly (1979) suggest that these events are very similar. Since frequent geodetic measurements were not done until recently, any analysis, such as done by Segall and Du (1993), using geodetic data for co-seismic displacements, is compromised, since those measurements include not only co-seismic

offset, but also inter-seismic and post-seismic signals. It is possible that the 1966 earthquake had the same initial rupture pattern as 1934, but may have had significant post-seismic slip southeast of Gold Hill. Continued measurements at Parkfield should be able to resolve whether or not post-seismic slip extends southeast of Gold Hill from the 2004 event.

The speed-up of fault slip over the 1993 to 1995 interval suggested by Gwyther et al. (1996), Langbein et al. (1999), Nadeau and McEvilly (1999), and Gao et al. (2000), as well as the occurrence of three $M > 4$ earthquakes from late 1992 to late 1994, perturbed the stresses under Middle Mountain (Fletcher and Gutteri, 1998 and Fletcher and Spudich, 1999). One scenario is that any of these $M4$ earthquakes could have been a potential foreshock to an eventual Parkfield earthquake with rupture starting under Middle Mountain. In both 1934 and 1966, $M5$ foreshocks preceded Parkfield mainshocks by 17 minutes. The three earthquakes with $M > 4$ in 1992-1994 occurred closer than three km southeast of the 1966 hypocenter, and all ruptured toward that point, but none was either a foreshock or grew into a $M6$ mainshock. Perhaps, the accelerated aseismic slip during 1993-1995, as suggested by the geodetic data and repeating earthquake data, may have relieved stress in the area of 1934 and 1966 hypocenter beneath Middle Mountain. Thus, strain continued to accumulate on the fault southeast of Middle Mountain until the 2004 event when the fault failed beneath Gold Hill.

When the detailed data from the 2004 Parkfield earthquake are analyzed more fully, the role of post-seismic slip within the earthquake cycle will be better defined. As noted in the discussion on source models, inclusion of the static GPS data with the seismic data tends to bias the slip distribution upwards. It is clear from the 2-hour GPS results and the strainmeter data shown in Figure 15 that, immediately after the mainshock, there is rapid, post-seismic deformation that adds to the co-seismic offset. Thus, it is perhaps not valid to mix the static, GPS data with the seismic waveform data to produce a model of rupture (Dreger, 1997). In contrast, the 1-second GPS waveform data plus the high-rate, 200 samples per second, dilatometer data provide consistent constraints on the rupture model since both of these instrument types can provide static offsets immediately after the passage of the seismic wave. Then, the slip distribution during the post-seismic period can be mapped using a combination of GPS and strainmeter data using the methods of Segall and Matthews (1997)

With regard to the evolution of surface slip in Parkfield earthquakes, the geologic observations and the creepmeter data both suggest that ground breakage did not necessarily occur simultaneously with the mainshock; rather slip appears to have occurred minutes to hours following the mainshock. In addition, at least relative to the strainmeter data, the time constant is longer for the creepmeter for post-seismic slip. This slower response suggests that the observed surface slip could be a manifestation of slip at depth loading the surface soils. In addition, the anomalous behavior of the CARH GPS site suggests that the assumption of simple, planar fault at the surface is not always valid. To the west of CARH, the SWFZ had its highest value of slip. But, as noted, the afterslip on the SWFZ is negligible. To the east of CARH, the San Andreas Fault had delayed surface rupture, but has had substantial post-seismic slip. Thus, the fault near CARH can perhaps be thought as a wide zone which accommodates slip. More study is required to understand this process.

The 2004 Parkfield earthquake occurred only 9 months after the 2003 M6.5 San Simeon earthquake, and only ~50 km away, possibly suggesting a causal relationship. The San Simeon mainshock loaded the San Andreas at Parkfield with 0.03-0.1 bars of Coulomb stress (Hardebeck et al., 2004), but there was no noticeable increase in seismicity rate, displacement rate, or strain rate on the San Andreas prior to the M6.0 mainshock.

Conclusions

The long-anticipated Parkfield earthquake finally occurred on 28 September 2004. Although characteristic in its rupture of the same 25 km segment of the San Andreas Fault and very similar in size to the 1922, 1934, and 1966 Parkfield events, it exhibited significant differences from those earlier events. In particular, while prior events initiated under Middle Mountain north of Parkfield and ruptured toward the southeast, the 2004 event nucleated beneath the area near Gold Hill south of Parkfield and ruptured northwest towards Middle Mountain. And, unlike the 1934 and 1966 events, this event was not preceded by any foreshocks ($M > 0$). The intensive monitoring of deformation and seismicity at Parkfield for the 20 years prior to the 2004 earthquake, during the earthquake, and now following the earthquake will continue to yield more insights into the physics of earthquakes.

Clearly, more work will be needed to obtain a better model of slip for the 2004 event. In particular, the strong motion data, discussed in Shakal et al., (this volume), will be incorporated in future slip models. In addition, partitioning between the co-seismic, dynamic rupture and the slower, but significant, post-seismic slip needs to be carefully taken into account. Finally, more study is needed to unravel the structure of the fault zone adjacent to Gold Hill and to understand the behavior of this part of the fault.

The data from highly sensitive, borehole strainmeters located near the hypocenter and very close to the eventual patch of fault that ruptured have placed an upper limit on the amount of slip that may have occurred pre-seismically. For the moderate-sized, Parkfield earthquake, these data indicate that the equivalent moment of pre-seismic slip is less than 10^{-4} of the seismic moment of the mainshock. This indicates that searching for precursors signal in strain and other deformation instruments will probably be so difficult as to render this an ineffective means of predicting earthquakes. It should be noted that there were two borehole strainmeters located just east of Gold Hill and close to the epicenter of the 2004 event, but they had both failed by the mid-1990s. Had these instruments been working, the limits on possible pre-seismic slip would have been better constrained.

The distribution of aftershocks to the 2004 event is similar to the background seismicity. However, the aftershocks tend to follow the SWFZ rather than the main, mapped trace of the San Andreas Fault. Future field experiments will indicate whether this deviation is an artifact of the velocity model, or if it does indicate the fault's location at depth.

At the time of writing this report, post-seismic deformation is continuing. Quantifying the release of strain-energy in the post-seismic period relative to the mainshock will be answered

as a result of continued monitoring with GPS, strainmeters, and creepmeters. The creepmeter measurements from 1966 suggest that the post-seismic period can be several years long (Smith and Wyss, 1968). Whereas those observations are sensitive to surface slip, the geodetic monitoring, currently being done at Parkfield, is sensitive to slip at depth.

Finally, except for the lack of ground breakage south of Gold Hill, the pattern of surface ground breakage is similar to that from the 1966 earthquake including rupture on the southwest fracture zone.

Contributors

Gerald Bawden, Shawn Devlin, William Ellsworth, Gary Fuis, Nancy King, Jim Lienkaemper, Jerry Svarc, Andy Michael, John Tinsley, Andy Snyder at USGS; Kyuhong Choi, Andria Bilich, Kristine M. Larson at University of Colorado at Boulder; Steve Park at UC Riverside; K. Clahan, A. Rosinski, W. Bryant, D. Branum at CGS; Ramon Arrowsmith and N. Toké at Arizona State University; Mark Murray and Denise Templeton at UC Berkeley; Yehuda Bock and Jeff Genrich, UC San Diego; and Michael Gladwin and Marie Mee at CSIRO.

Acknowledgments

The list is long of people who contributed a significant part of the careers devoted to the Parkfield experiment. Consequently, we will provide a short list. Instrumental in conceiving the experiment are Al Lindh, Bill Bakun, Tom McEvelly and John Filson; those who actually built the experiment but have moved onto other endeavors include Bob Burford, Sandy Schulz, Rich Leichti, Duane Hamann, Peter Malin, Don Lippert, Ross Gwyther, Rhodes Hart, Brett Baker, Jim Wilmesher, Carl Mortensen, John Sims, Bob Mueller, Larry Slater, and Andy Records; and those who have been diligently maintaining the experiment include Andy Snyder, Chris Dietel, Doug Myren, Gary Hamilton and crew, David Oppenheimer, Tom Burdette and crew, Rich Clymer, Stuart Wilkinson, Larry Baker, and Russel Sell. Discussions with Bill Bakun and Ruth Harris along with reviews by Art McGarr, Evelyn Roeloffs and William Ellsworth helped considerably.

References

- Bakun, W.H., Focal depth of the 1966 Parkfield, California, earthquakes, *JGR*, 77, 3816-3822, 1972,
- Bakun, W.H., and T.V. McEvelly, Earthquakes near Parkfield, California: Comparing the 1934 and 1966 sequences, *Science*, 205, 1375-1377, 1979.
- Bakun, W.H., and T.V. McEvelly, Recurrence models and Parkfield, California, earthquakes, *J. Geophys. Res.*, 89, 3051-3058, 1984.

Bakun, W.H., and A.G. Lindh, The Parkfield, California earthquake prediction experiment, *Science*, 229, 619-624, 1985.

Borcherdt, R.D., M. J.S. Johnston, C. Dietel, G. Glassmoyer, D. Myren, and C. Stephens, Acceleration and Volumetric Strain generated by the Parkfield 2004 Earthquake as Recorded on the General Earthquake Observation System (GEOS) Strong-Motion Array near Parkfield, CA., U.S. Geological Survey Report, Open-File Report Number 2004-1376, 74 pp. 2004.

Brown, R. D., Jr., J. G. Vedder, R. E. Wallace, E. F. Roth, R. F. Yerkes, R. O. Castle, A. O. Waananer, R.W. Page, and J.P. Eaton (1967). The Parkfield-Cholame, California earthquakes of June-August 1966-Surface geologic effects, water-resources aspects, and preliminary seismic data, U.S. Geol. Surv. Profess. Paper 579, 66 pp., 1967.

Ben-Zion, Y., J.R. Rice, and R. Dmowska, Interaction of the San Andreas Fault creeping segment with adjacent great rupture zones and earthquake recurrence at Parkfield, *J. Geophys. Res.*, 98 (B2), 2135-2144, 1993.

Eberhart-Phillips, D., and A.J. Michael, 1993, Three-dimensional velocity structure and seismicity in the Parkfield region, central California, *J. Geophys. Res.*, 98, 15,737-15,758.

Evans, J. R., D. Eberhart-Phillips, C. H. Thurber, User's manual for SIMULPS12 for imaging v_p and v_p/v_s ; a derivative of the "Thurber" tomographic inversion SIMUL3 for local earthquakes and explosions, U. S. Geological Survey Open-File Report: OF 94-0431, 101 pp., 1994.

Dreger, D. S. , The large aftershocks of the Northridge earthquake and their relationship to mainshock slip and fault-zone complexity, *Bull. Seism. Soc. Am.*, 87, 1259-1266, 1997

Fletcher, J.B., L.M. Baker, P. Spudich, P. Goldstein, J.D. Sims, and M. Hellweg, The USGS Parkfield, California, dense seismograph array:UPSAR, *Bull. Seism. Soc. Amer.*, 82, 1041-1070, 1992.

Fletcher, J.B., and P. Spudich, Rupture characteristics of the three M 4.7 (1992-1994) Parkfield earthquakes, *J. Geophys. Res.*, 103, 835-854, 1998.

Fletcher, J.B., and M. Guatteri, Stress Drop for three M ~ 4.3-4.7 (1992-1994) Parkfield, CA, earthquakes, *Geophys. Res. Lett.*, 26 (15), 2295-2298, 1999.

Frankel, A., S. Hough, P. Frieberg, and R. Busby, Observations of Loma Prieta aftershocks from a dense array in Sunnyvale, California, *Bull. Seism. Soc. Amer.*, 81, 1900-1922, 1991

Gao, S., P.G. Silver, and A.T. Linde, Analysis of deformation data at Parkfield, California: Detection of a long-term strain transient, *J. Geophys. Res.*, 105 (B2), 2955-2967, 2000.

Gwyther, R.L., M.T. Gladwin, M. Mee, and R.H.G. Hart, Anomalous tensor strain at Parkfield during 1993-1994, *Geophys. Res. Lett.*, 23, 2425-2428, 1996.

Hardebeck, J. L., J. Boatwright, D. Dreger, R. Goel, V. Graizer, K. Hudnut, C. Ji, L. Jones, J. Langbein, J. Lin, E. Roeloffs, R. Simpson, K. Stark, R. Stein, J. C. Tinsley, Preliminary Report on the 22 December 2003 M6.5 San Simeon, California, Earthquake, *Seism. Res. Lett.*, 75, 155-172, 2004.

Harris, R.A., and R.J. Archuleta, Slip budget and potential for M7 earthquake in Central California, *Geophys. Res. Lett.*, 15, 1215-1218, 1988.

Hartzell, S. H., and T. H. Heaton, Inversion of strong ground motion and teleseismic waveform data for the fault rupture history of the 1979 Imperial Valley, California, earthquake, *Bull. Seism. Soc. Am.*, 73, 1553-1583, 1983

Ji, C., D.J. Wald, and D.V. Helmberger, Source description of the 1999 Hector Mine, California earthquake; Part I: Wavelet domain inversion theory and resolution analysis, , Vol 92, No. 4. pp. 1192-1207, 2002.

Kanamori, H. and D.L. Anderson, 1075. Theoretical Basis of some Empirical Relations in Seismology, *Bull. Seis. Soc. Am.*, 65, 1073-1096, 1975

Langbein, J., R. Gwyther, R. Hart, and M.T. Gladwin, Slip rate increase at Parkfield in 1993 detected by high-precision EDM and borehole tensor strainmeters, *Geophys. Res. Lett.*, 26, 2529-2532, 1999.

Langbein, J. and Y. Bock, High-rate real-time GPS network at Parkfield; Utility for detecting fault slip and seismic displacements, *Geophys. Res. Lett.*, 31, 2004.

Larson, K.M, P. Bodin, and J. Gomberg. Using 1-Hz GPS data to measure deformation caused by the Denali fault earthquake, *Science*, 300(5624), 1421-1424, 2003.

Lienkaemper, J. J. and R. D. Brown, Jr., Map of faulting accompanying the 1966 Parkfield earthquake, U.S. Geol. Surv. Open-File Rept. 85-661, 3 sheets, scale 1:12,000., 1985.

Lindh, A.G. and D.M. Boore , Control of rupture by fault geometry during the 1966 Parkfield Earthquake, *Bull. Seis. Soc. Amer.*, 71, 95-116. (1981)

Meltzner, A.J, and D.J. Wald, Foreshocks and aftershocks of the great 1857 California earthquake, *Bull. Seism. Soc. Am.*, 89, 1109-1120, 1999

Michael, A. J., and Eberhart-Phillips, D. M., 1991, Relationships between Fault Behavior, Subsurface Geology, and Three-Dimensional Velocity Models, *Science*, 253, 651-654.

Murray, J.R., P. Segall, P. Cervelli, W. Prescott, and J. Svarc, Inversion of GPS data for

spatially variable slip-rate on the San Andreas Fault near Parkfield, CA., *Geophys. Res. Lett.*, 28, 359-362, 2001,

Nadeau, R. M. and L. R. Johnson, Seismological Studies at Parkfield VI: Moment Release Rates and Estimates of Source Parameters for Small Repeating Earthquakes, *Bull. Seism. Soc. Am.*, 88, 790-814, 1998.

Nadeau, R.M. and T.V. McEvilly, Fault slip rates at depth from recurrence intervals of repeating microearthquakes, *Science*, 285, 718-721, 1999.

Nadeau, R.M., A. Michelini, R.A. Uhrhammer, D. Dolenc, and T.V. McEvilly, Detailed kinematics, structure and recurrence of micro-seismicity in the SAFOD target region, *Geophys. Res. Lett.*, 31, 2004.

Park, S.K., Monitoring resistivity changes in Parkfield, California: 1988-1995, *J. Geophys. Res.*, 102 (B11), 24,545-24,559, 1997.

Pasyanos, M.E., D.S. Dreger, and B. Romanowicz, Toward Real-Time Estimation of Regional Moment Tensors, *Bull. Seism. Soc. Amer.*, 86, 1255-1269, 1996.

Roeloffs, E., and J. Langbein, The earthquake prediction experiment at Parkfield, California, *Reviews of Geophysics*, 32 (3), 315-336, 1994.

Segall, P., and Y. Du, How similar were the 1934 and 1966 Parkfield earthquakes?, *J. Geophys. Res.*, 98, 4527-4538, 1993.

Segall, P, and M. Matthews, Time-dependent inversion of geodetic data, *J. Geophys. Res.*, 98, 4527-4538, 1997.

Sieh, K.E, and R.M. Jahns, Holocene activity on the San Andreas Fault at Wallace Creek, California, *Geol Soc. Am. Bull.*, 1984, 2283-2395, 1984.

Simpson, R.W., S.S. Schulz, L.D. Dietz, and R.O Burford, The response of the creeping parts of the San Andreas Fault to earthquakes o nearby faults: Two examples, *Pure Appl. Geophys.*, 126, 665-685, 1988.

Smith, S.W., and M. Wyss, Displacement of the San Andreas Fault subsequent to the 1966 Parkfield earthquake, *Bull. Seismol. Soc. Am.*, 58, 1955-1973, 1968.

Thurber, C., S. Roecker, K. Roberts, M. Gold, L. Powell, and K. Rittger, Earthquake locations and three dimensional fault zone structure along the creeping section of the San Andreas Fault near Parkfield, CA: Preparing for SAFOD, , Vol, 30, No., 3, 1112., doi:10.1029/2002GL016004, 2003.

Toda, S., and R.S. Stein, Response of the San Andreas Fault to the 1983 Coalinga-Nunez

Earthquakes: An application of interaction-based probabilities for Parkfield, *J. Geophys. Res.*, 107, 2002.

Waldhauser, F. and Ellsworth, W. L., A double-difference earthquake location algorithm; method and application to the northern Hayward Fault, California, *Bull. Seism. Soc. Am.*, 90, 1353-1368, 2000.

Waldhauser, F., W.L. Ellsworth, D.P. Schaff, and A. Cole, High-resolution spatio-temporal behaviour of Parkfield Seismicity, *Geophys. Res. Lett.*, 31, (2004).

Figure Captions

Figure 1. A map of Central California showing the San Andreas Fault near Parkfield and the locations of the 2004 Parkfield earthquake, the 1966 Parkfield earthquake, major faults, major roads, major towns, and some geographic features near Parkfield. The location of EarthScope's San Andreas Fault observatory at depth (SAFOD) is located. Inset shows general location of Parkfield within the State of California.

Figure 2. Locations of many of the instruments used to monitor crustal deformation at Parkfield.

Figure 3. Comparison of Wood-Anderson records from the N components of the stations MHC (Mt. Hamilton) and SBC (Santa Barbara) for the 1934, 1966 and 2004 Parkfield earthquakes. The upper traces are taken from Bakun and McEvelly (1979) and show recordings from 1934 (dashed) and 1966 (solid). The lower traces for the 2004 earthquake were simulated from broadband recordings from an STS-1 seismometer (MHC) and an STS-2 seismometer (SBC). In these records, only the early arrivals are shown; the S-wave would arrive well after the time interval shown.

Figure 4. Map view of relocated seismicity near Parkfield. Aftershocks of the 2004 Parkfield earthquake are shown in black, background seismicity 1969-2004 in gray. The 2004 mainshock is indicated by a star. Black lines indicate the mapped surface trace of the San Andreas, including the main trace and the SWFZ. Boxes indicate cross sections in Figure 5. Double-couple focal mechanisms obtained from moment tensor inversion of long-period (50 to 20 sec) regional data of the BDSN are plotted in the first 48 hours after the earthquake.

Figure 5. Cross sections (top), and along-fault depth section (bottom), of relocated seismicity near Parkfield. Aftershocks of the 2004 Parkfield earthquake are shown in black, background seismicity 1969-2004 in gray. The 2004 mainshock is indicated by a star. Locations of cross sections shown in Figure 4. No vertical exaggeration.

Figure 6: Map showing locations of ground breakage observed from the 28 September 2004, Parkfield earthquake.

Figure 7. Borehole strainmeter data (volumetric strain) at 5 sites for the 10 day prior to the mainshock. The light blue line are the strainmeter data corrected for the changes in atmospheric pressure. The heavier lines are same data but with the earth tide signal removed. Contraction is reckoned positive.

Figure 8. Borehole strainmeter data from one instrument, VC, for the 20 seconds period before the mainshock. Origin time of the 2004 mainshock and the time of the P-wave arrival are noted.

Figure 9. Three models of the slip distribution obtained from the inversion of geodetic,

strainmeter, and seismic data. The data used for each model are described in the text. The figure shows a cross section of the fault looking at the plane from the southwest. The symbols MM, CH, and GH show where the geographic features, Middle Mountain, Carr Hill, and Gold Hill project on the fault. Contours represent estimate slip in centimeters. In A), the model is obtained from inverting a combination of GPS and strainmeter data. - The mainshock hypocenter is given by the star. The size of the aftershock symbols are scaled to a 3 Mpa stress drop. In B), the model is obtained from inverting a combination of broadband seismic waveform data and GPS data. Aftershocks in the first 48 hours are plotted as black dots. The hypocenter is shown as a star, and the location of the 1966 mainshock is shown as the large circle. And, in C), the model is obtained from inverting some broadband and strong motion waveform data, 1 second displacement data from GPS, and offsets determined from GPS data. The aftershocks are plotted in black circles whose radii are normalized by its magnitude ($10^{M/2}$).

Figure 10. Locations of the GPS sites used to obtain Model 1 described in the text. The black arrows are the measured offsets and the gray arrows are the predicted offsets from the model. The ellipses represent the 95% error level of the data. The continuous GPS sites are shown with filled triangles and the campaign sites are shown with open triangles. The locations of the strainmeters are shown with squares. The location of the modeled fault is shown with a heavy line.

Figure 11. Record of dilatational strain and acceleration for the site FR which is identified in Figure 2. The strain record on top consists of 10-minute sampled data where the second trace is a 200 samples per second recording of the strain for 15 seconds spanning the mainshock. The bottom three traces are for a collocated accelerometer.

Figure 12. Data from a low sensitivity creepmeter at XMBC, the fault parallel displacement at the LAND GPS site, and the dilatational strain from the borehole strainmeter at FR. These three instruments are located near the northwest part of the rupture zone and are identified in Figure 2. Rather than using estimates of position averaged over a day, the GPS time-series is for 30-minute averages; by using shorter time intervals, this does increase the scatter in the observations. However, with the higher temporal resolution for the GPS, it is possible to compare its record with those from creepmeters and strainmeters since these are sampled every 10 minutes.

Figure 13. Data from the creepmeters spanning the time of the earthquake showing the delay of surface slip following the mainshock. Creepmeters XMM1 and XMBC, and XTA1 and TABC are each collocated with XMBC and XTA1 being low sensitivity but having a greater range than XMM1 and XTA1. Missing data from XMM1, XTA1, and CRR1 are caused by the slip exceeding the range of the sensors.

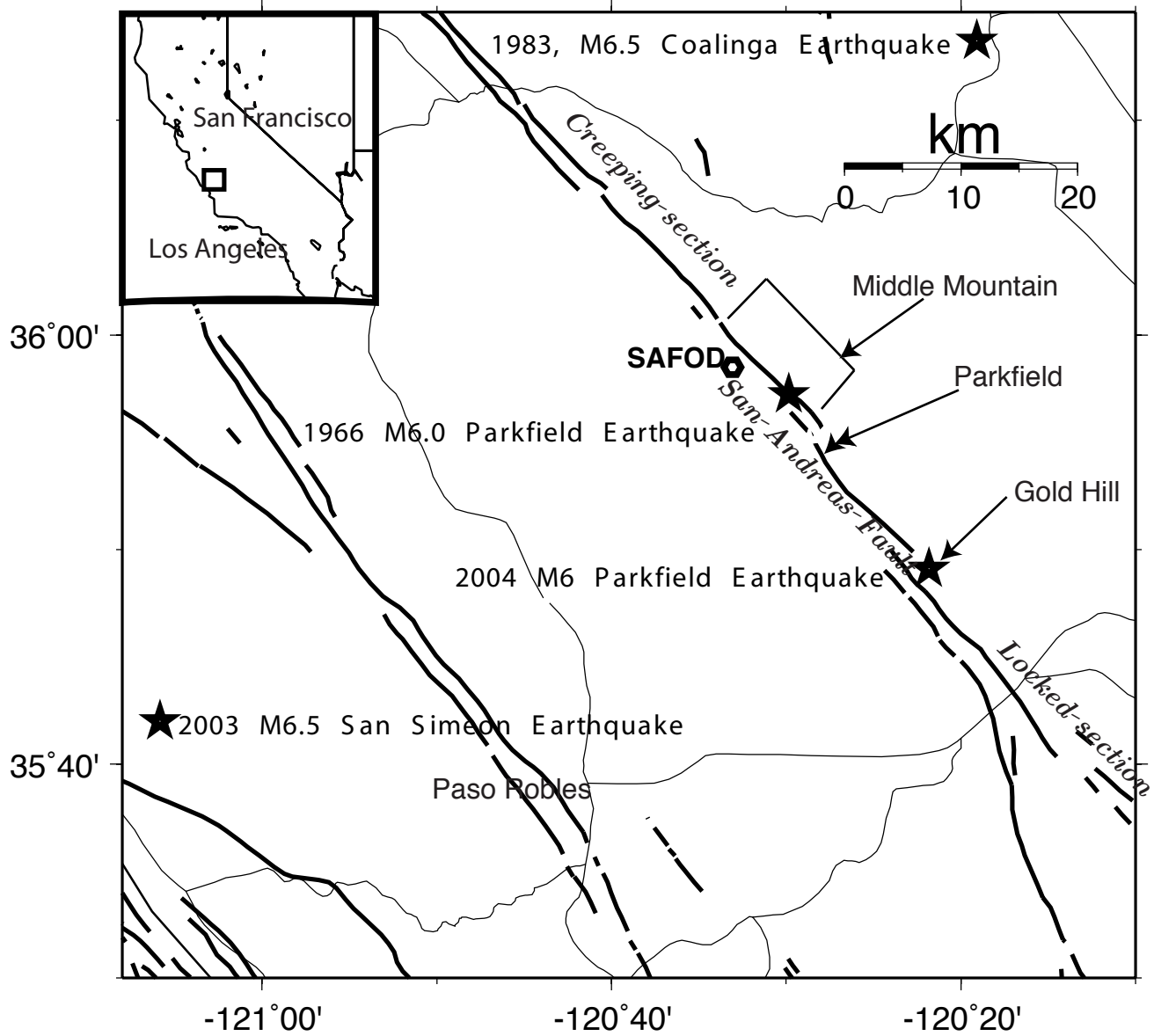


Figure 1

Monitoring sites

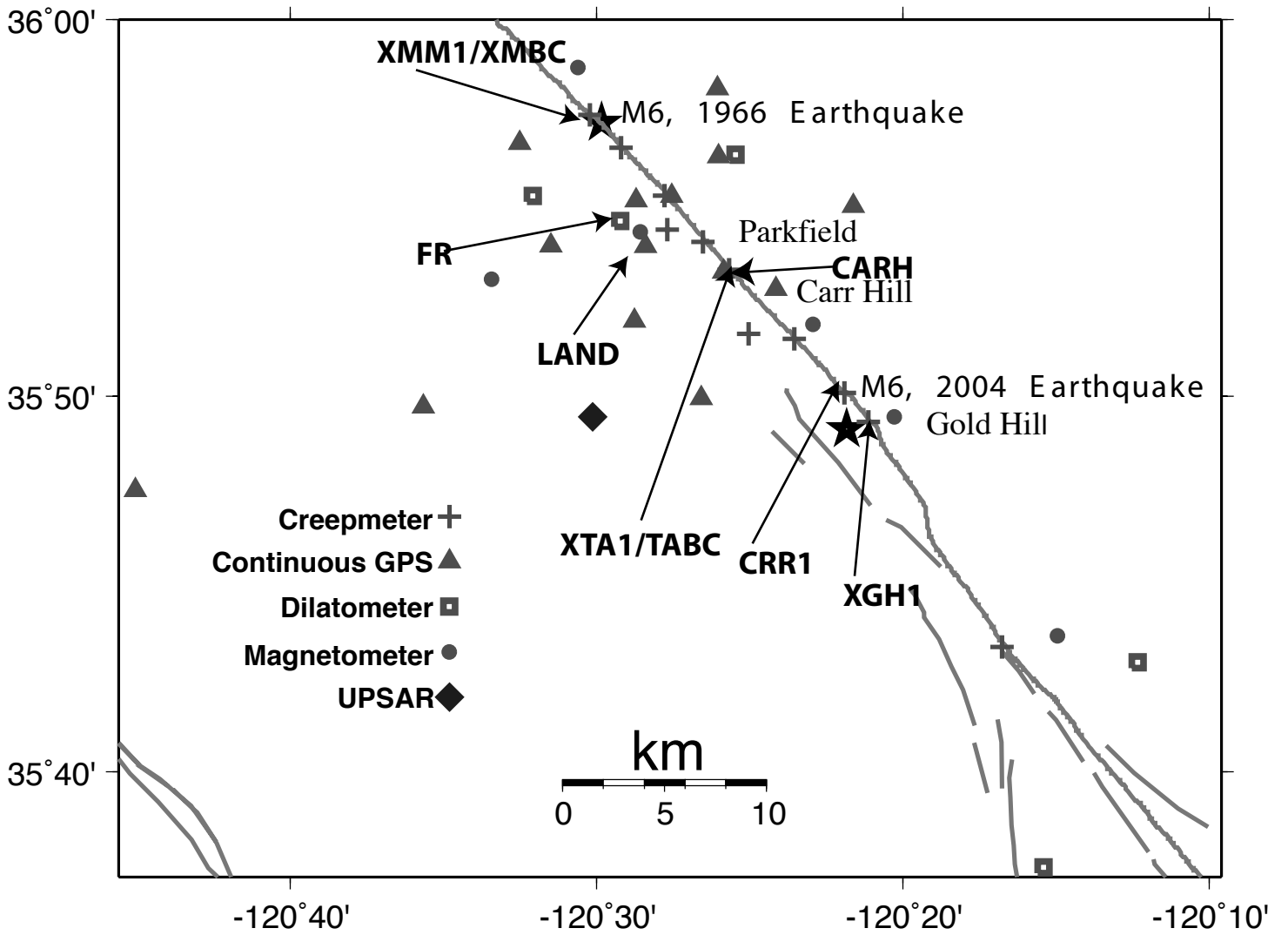


Figure 2

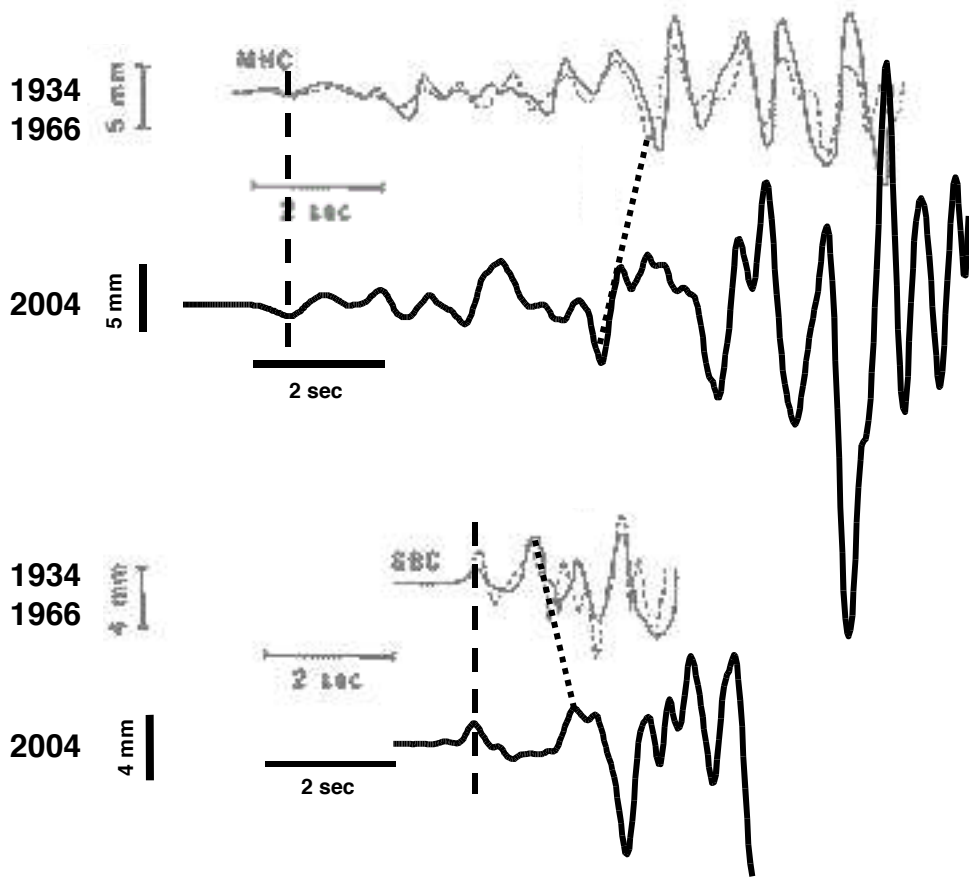


Figure 3

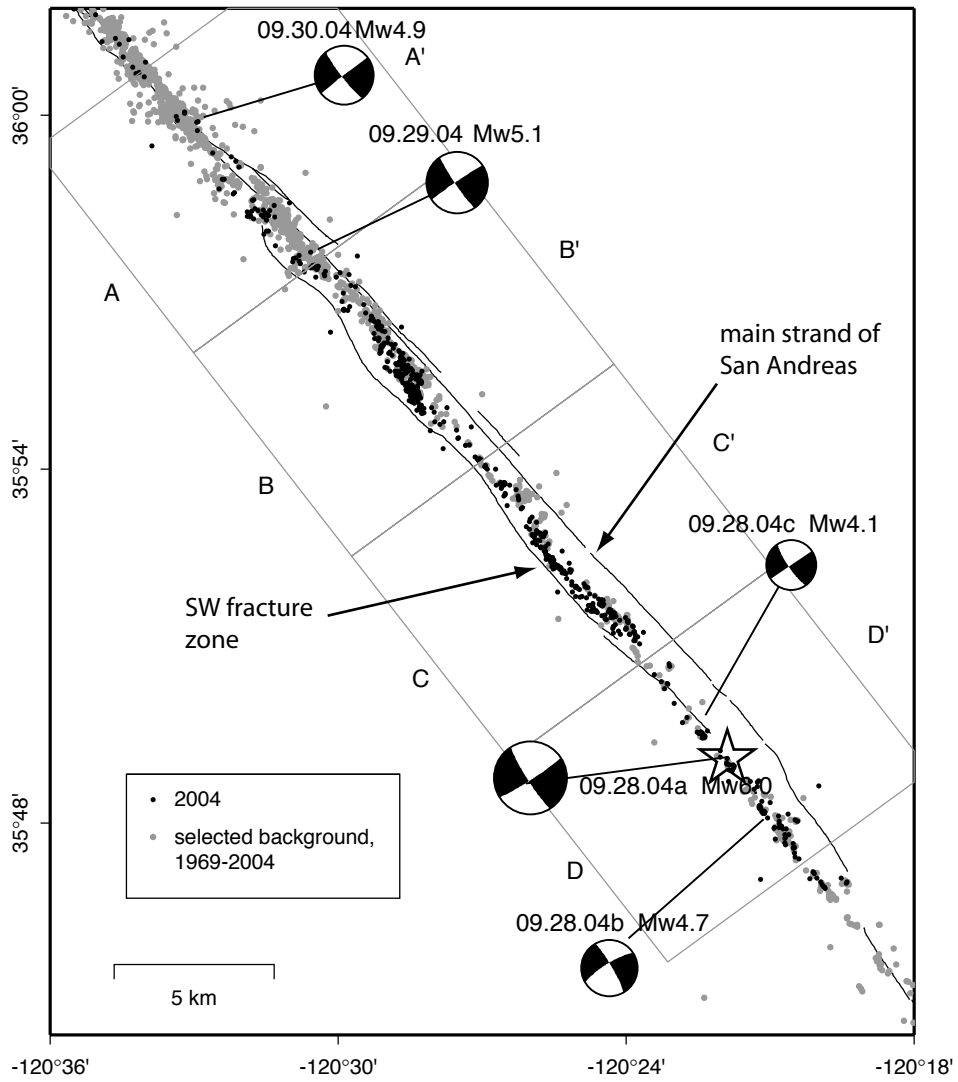


Figure 4

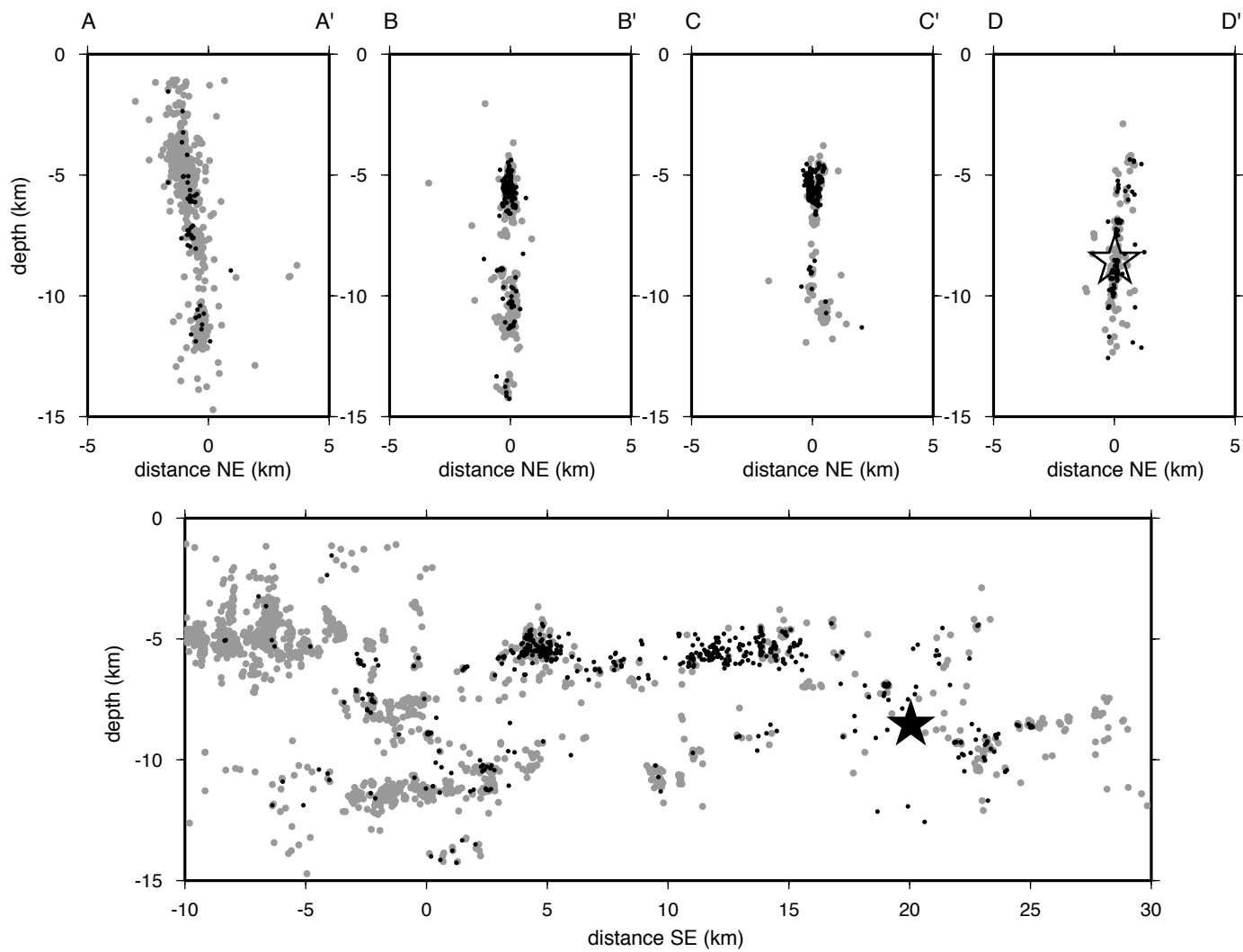


Figure 5

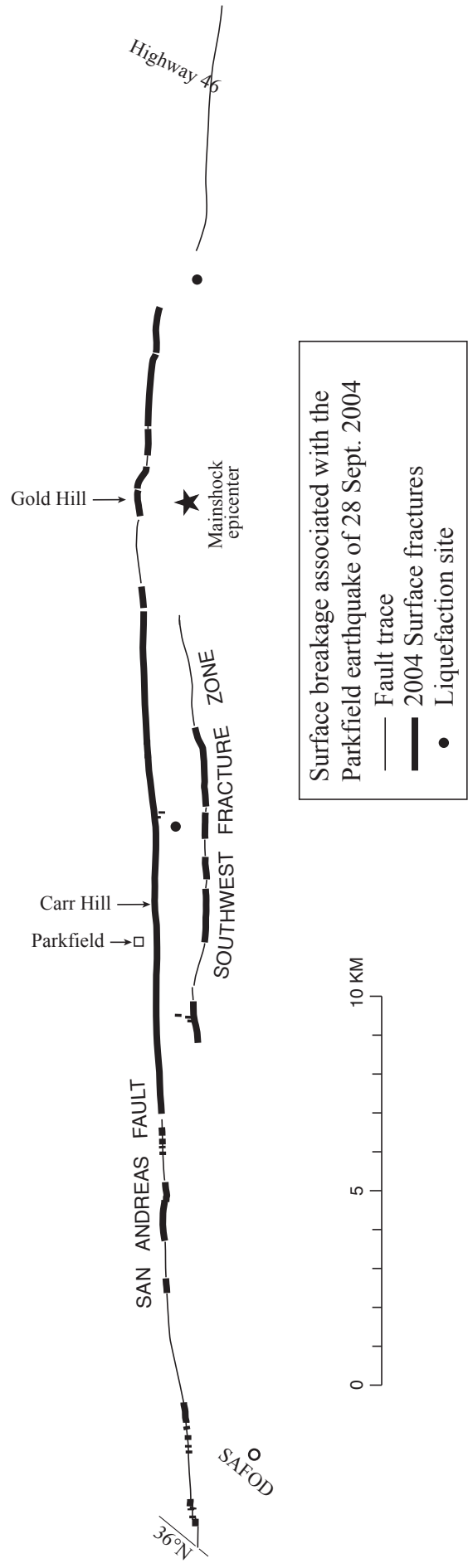


Figure 6

Parkfield M6
Earthquake

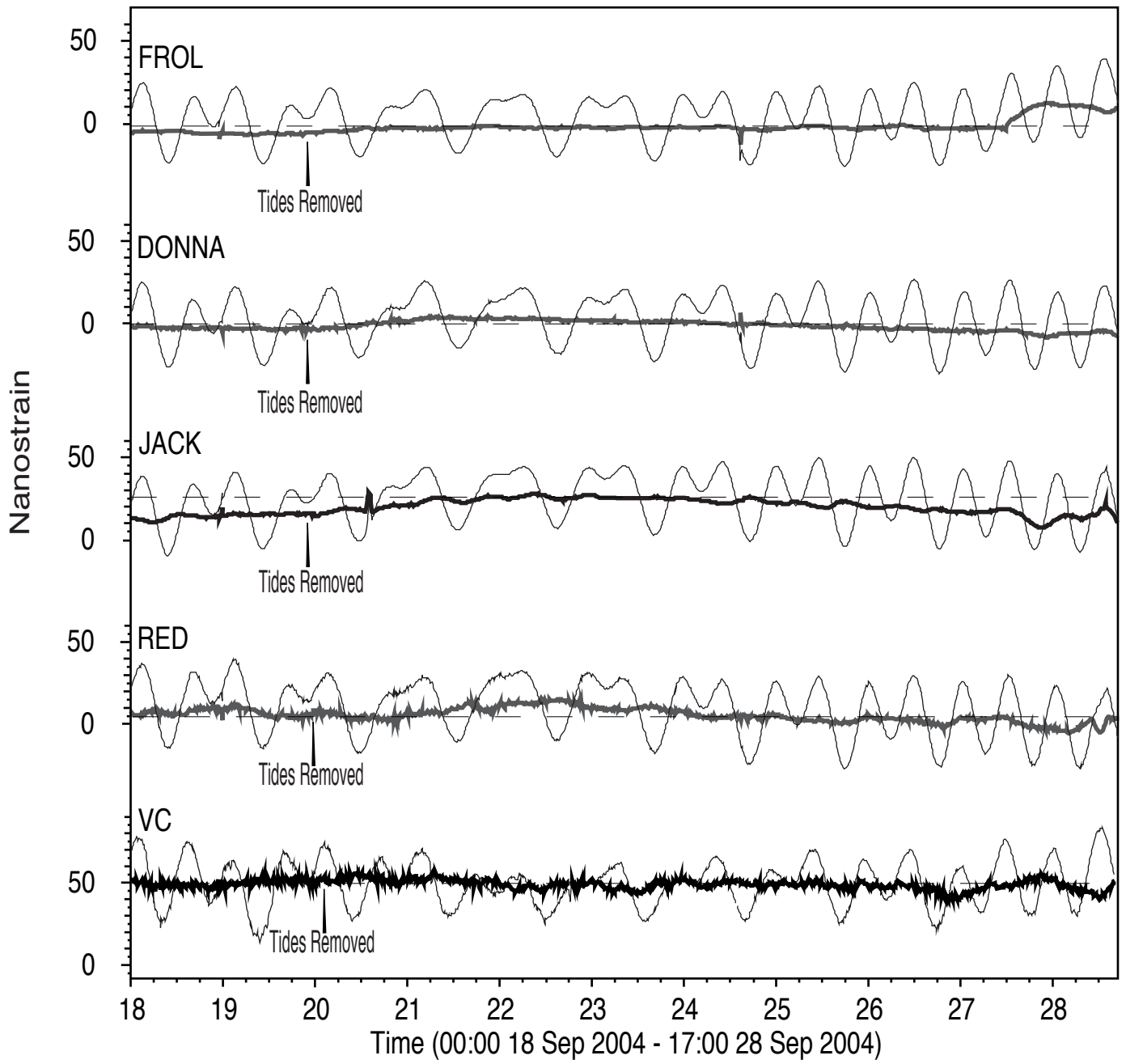


Figure 7

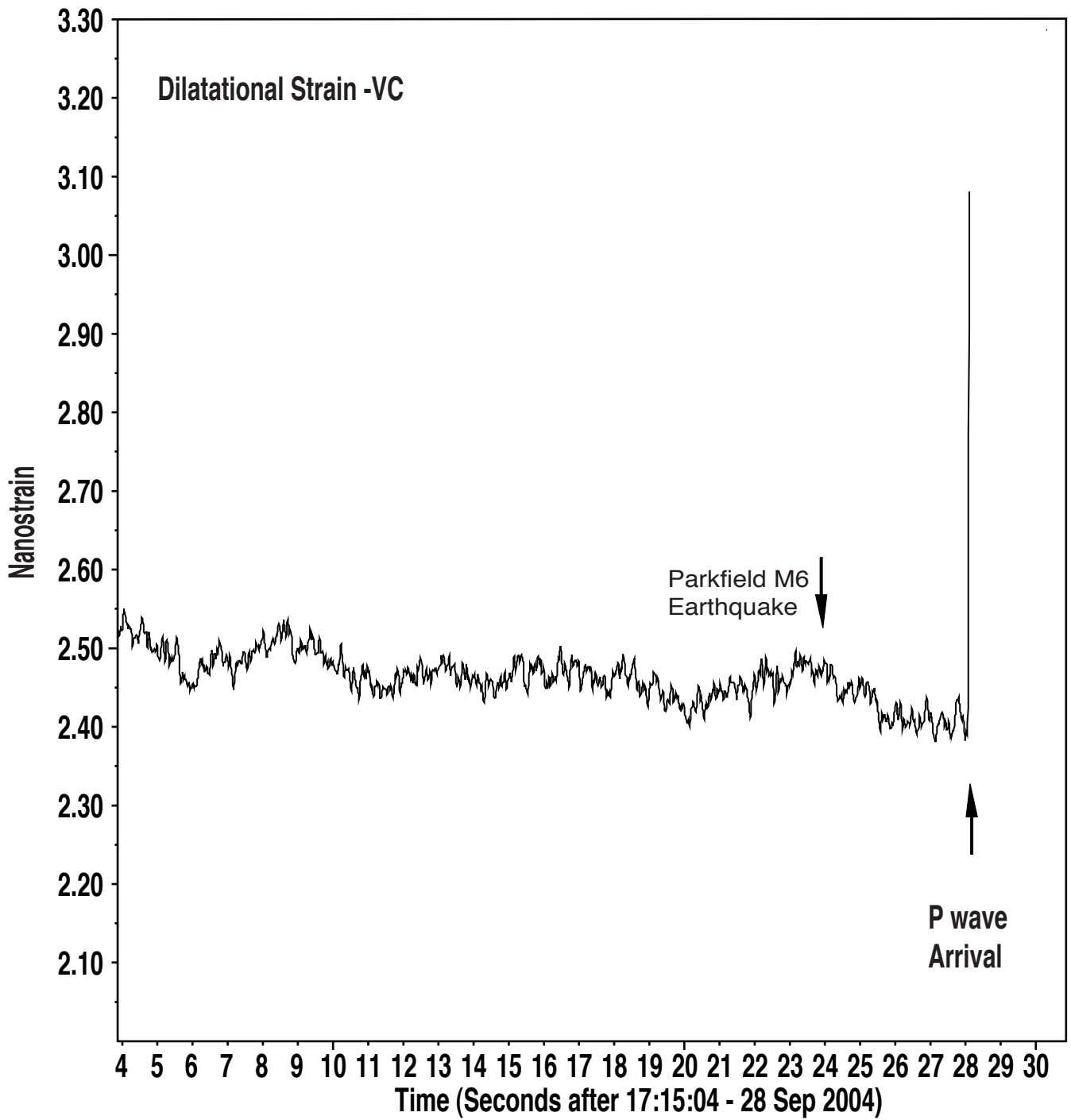
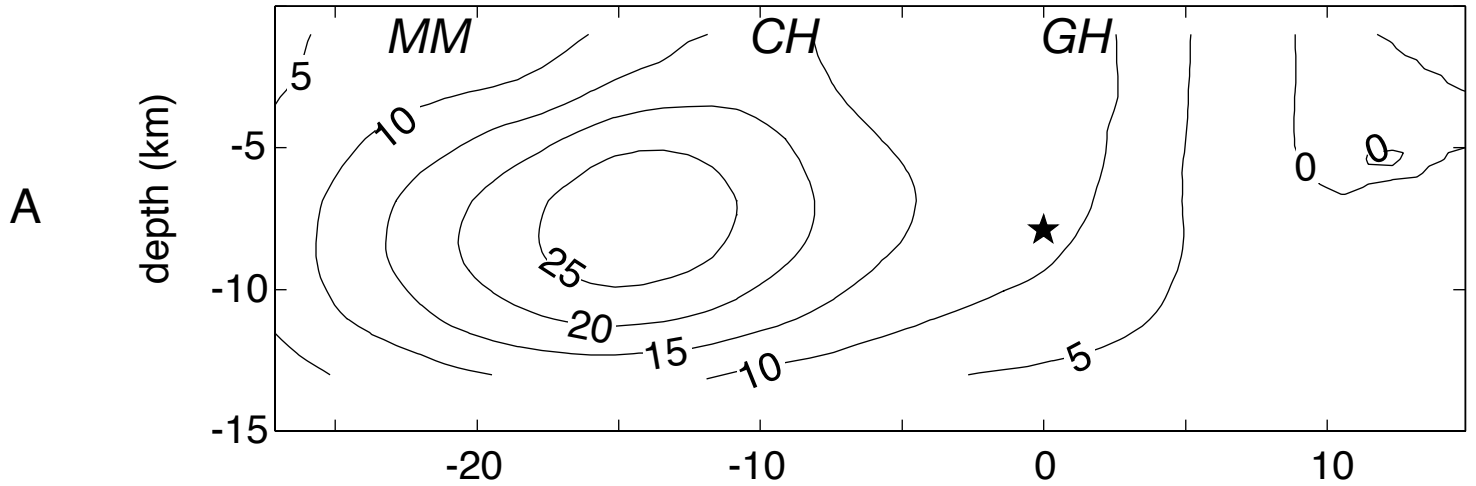
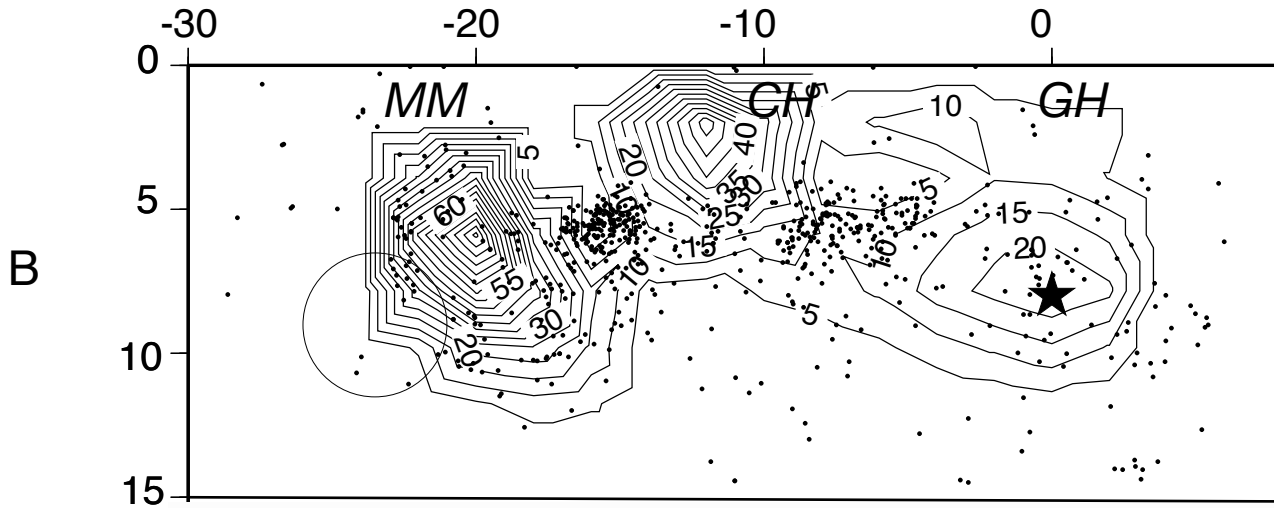


Figure 8

Model 1: using static GPS and strainmeter data



Model 2: using static GPS and seismic waveform data



Model 3: using static GPS, 1-Hz GPS and seismic waveform data

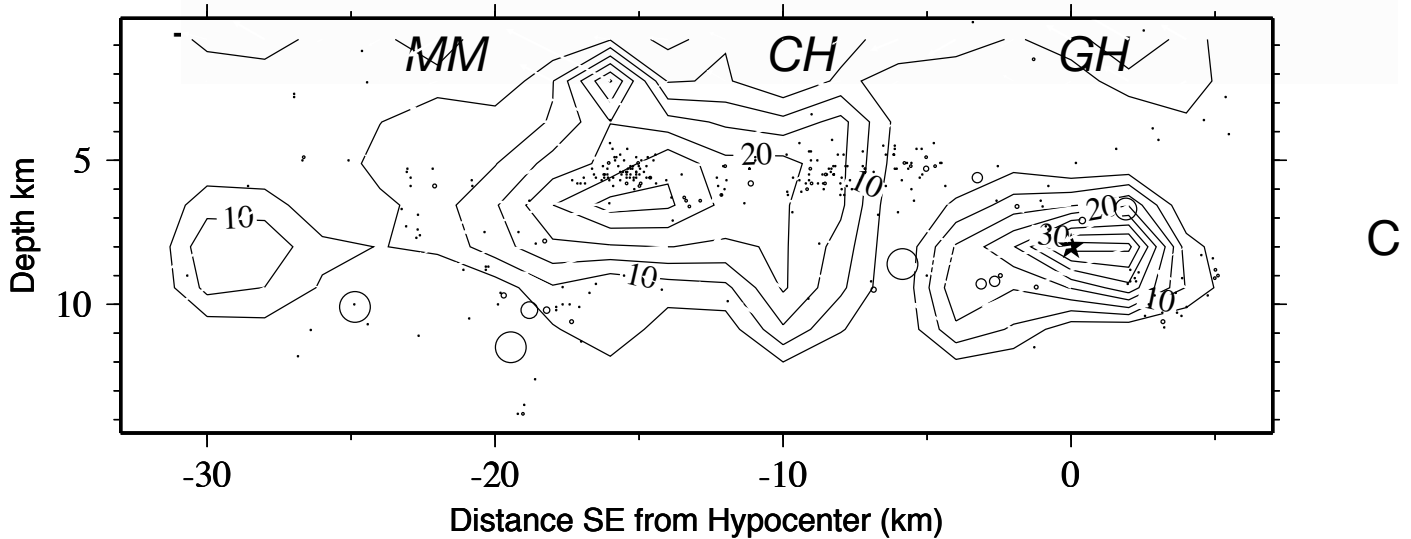


Figure 9

Observed (black) and estimated (grey) GPS displacements

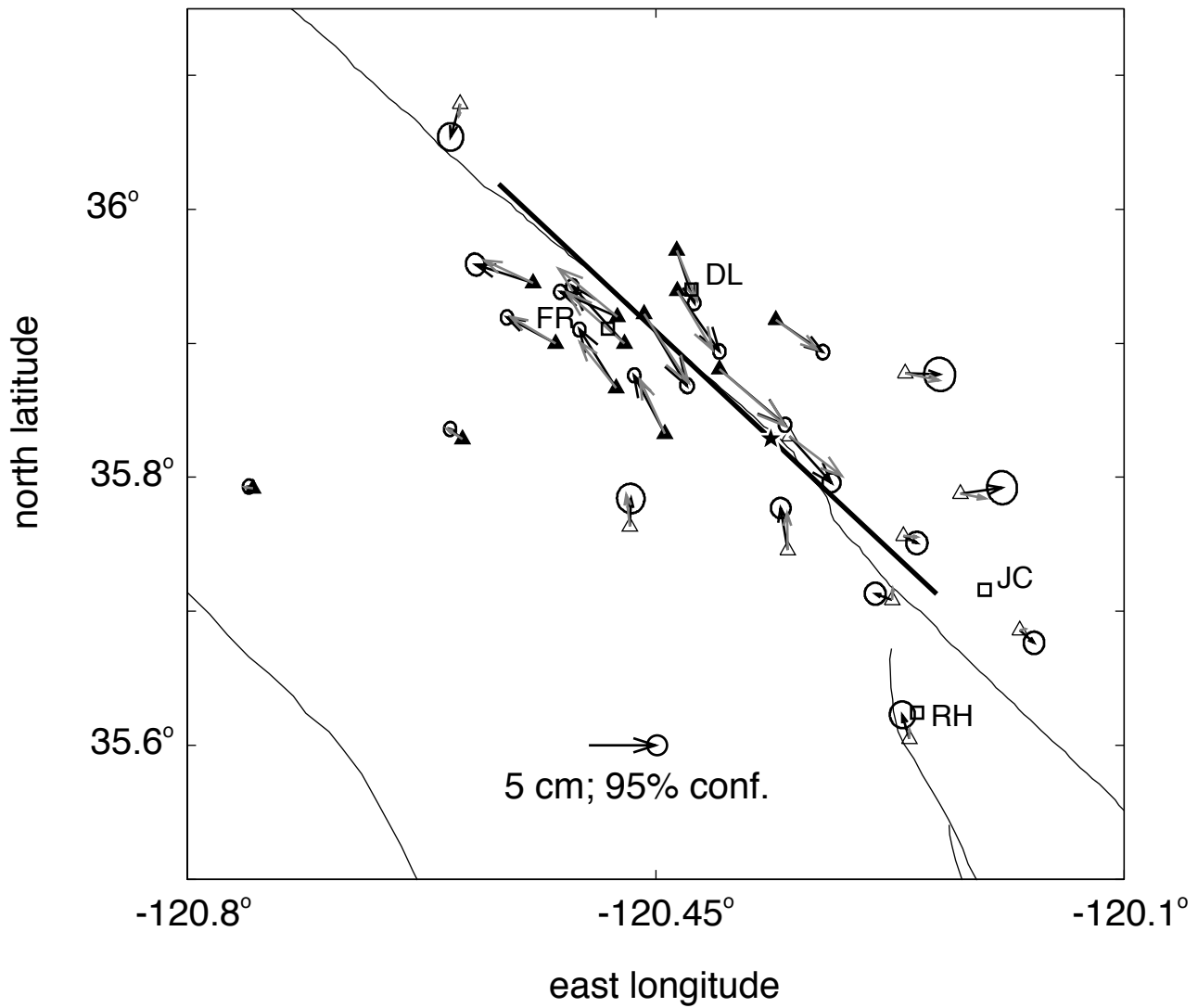


Figure 10

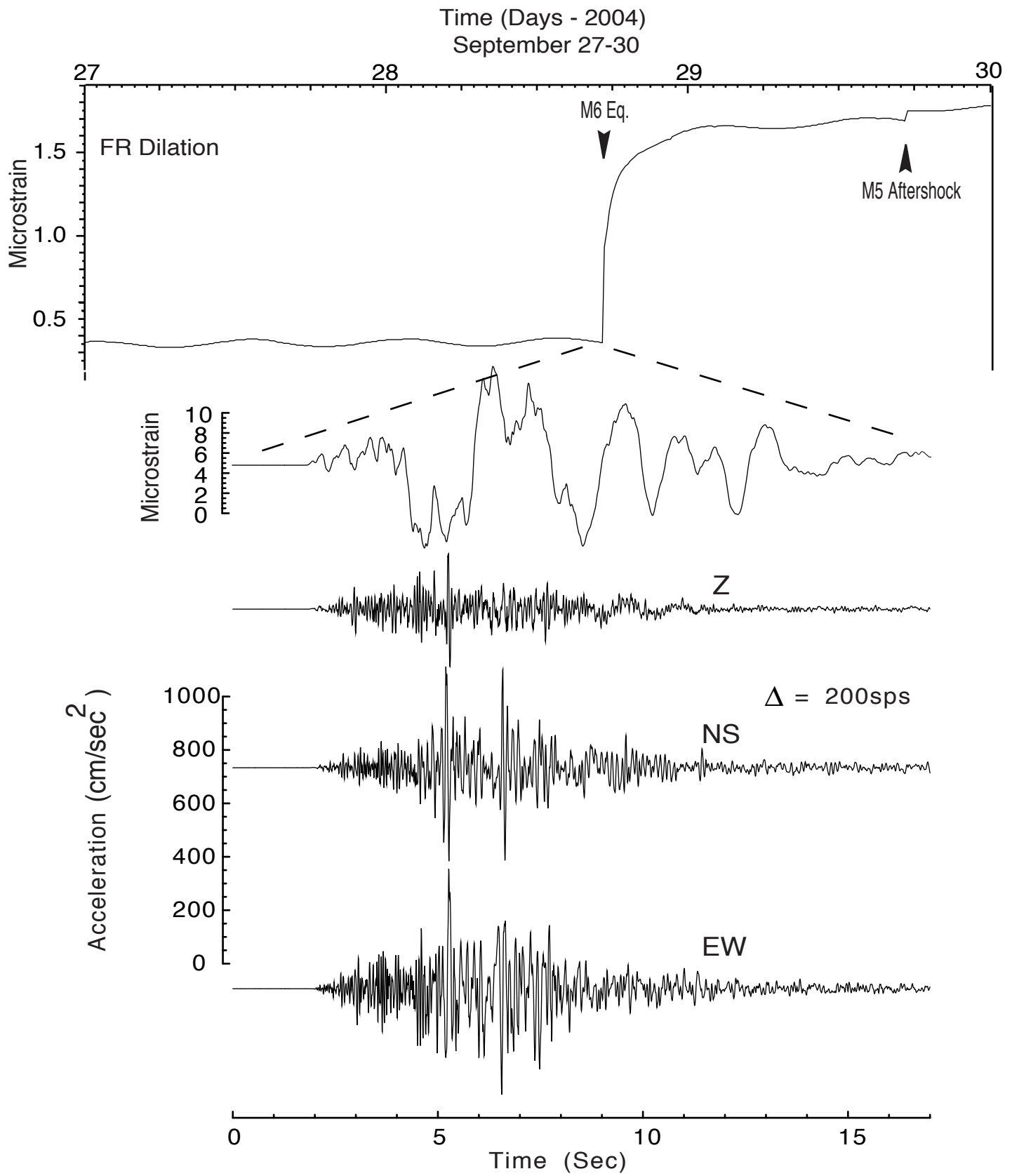


Figure 11

Co-seismic and Post-seismic creep, strain, and GPS

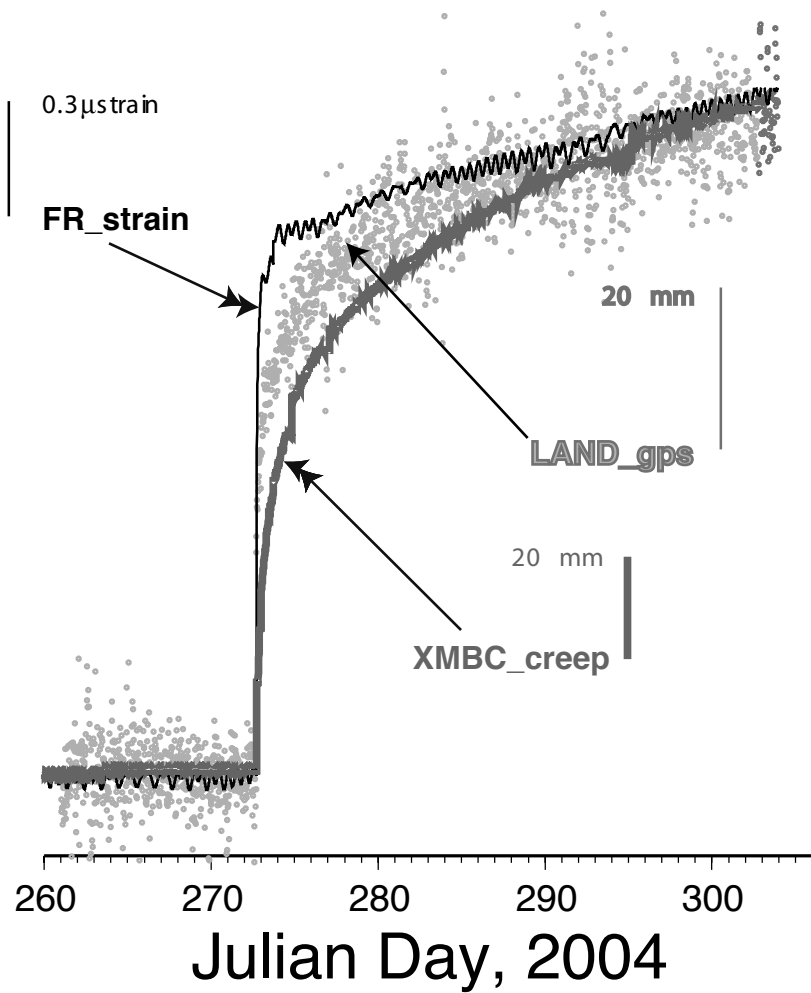


Figure 12

Creep data

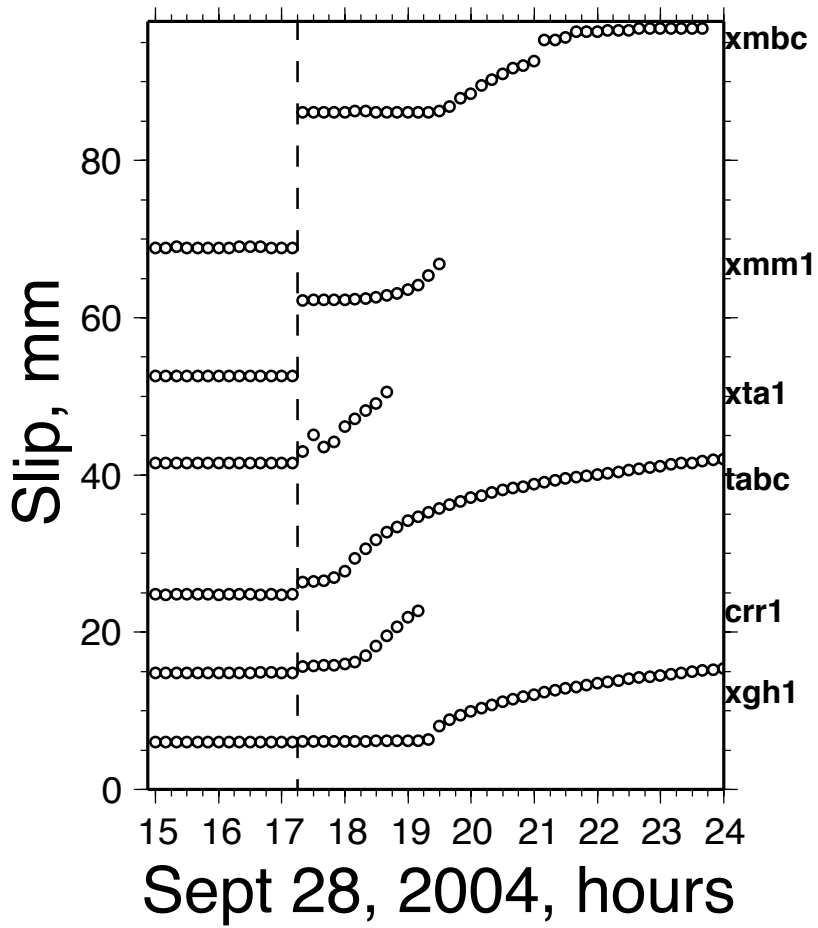


Figure 13